NUMERICAL DESCRIPTION OF PARTICLE AND BUBBLE MOTION IN THE SUBMERGED ENTRY NOZZLE REGION DURING STEEL CONTINUOUS CASTING

Claudia Pfeiler*; Andreas Ludwig; Menghuai Wu

Christian-Doppler Laboratory for Multiphase Modelling of Metallurgical Processes,
Department of Metallurgy, University of Leoben,
A - 8700 Leoben, Franz-Josef-Str. 18, Austria

Abstract

During continuous casting of steel several possibilities to reduce the amount of non-metallic inclusions in the melt exist. However, it is almost impossible to avoid them totally. If they become trapped in the solidified strand they can cause major quality problems in the final casting product. An engineering solution to avoid negative pressure in the nozzle, and so to inhibit the attraction of ambient air, is to inject argon gas at the stopper rod. Therefore, the steel melt may interact with both, non-metallic inclusions and argon gas bubbles mainly within the submerged entry nozzle and also in the mold area. The present study uses an Eulerian-Lagrangian approach to model the 3D turbulence (k-ε) flow of melt and the trajectories of individual non-metallic inclusions and gas bubbles in the nozzle region of a steel continuous caster. Two different methods to consider the momentum exchange between the melt and inclusions/bubbles are studied and compared. The uncoupled method considers only the impact of the melt flow on the trajectories of the inclusions/bubbles. In the coupled method bidirectional influences are considered. It is indicated that it is necessary to couple the bidirectional interactions between the melt and inclusions/bubbles to get realistic results, especially when large bubbles are present.

Keywords: turbulence, continuous casting, submerged entry nozzle, inclusion, bubble, discrete phase

1. Introduction

During continuous casting non-metallic inclusions and argon gas bubbles are brought/injected into the mould. Non-metallic inclusions are originated from deoxidation, reoxidation and exogenous processes, while argon gas bubbles are intentionally injected into the nozzle to prevent clogging and to avoid attraction of ambient air [1, 2]. The main concern related to the existence of non-metallic inclusions and gas bubbles is their transport in the molten pool. If the flow pattern is carefully adjusted by an optimized submerged entry nozzle (SEN) and/or optimized casting parameters, the melt flow may carry the inclusions and bubbles to the top surface, where they might be removed into the liquid slag layer. Otherwise,

*Corresponding author
" Tel: +43/3842/402 2225; Fax: +43/3842/402 2202.
E-mail address: claudia.pfeiler@mu-leoben.at".

they will eventually be trapped by the solidification front and cause defects in the final product. The transport of inclusions and bubbles depends obviously on the flow. Therefore, great modeling efforts were made to study the melt flow in the molten pool [1, 3-6] and, very recently, also to investigate directly the influence of the flow on the transport of inclusions [7-14]. Most of these publications consider only the uncoupled way, i.e. the melt flow impacts the trajectories of the inclusions, while the influence of the inclusions on the flow is ignored. However, a comprehensive model should consider bidirectional interactions between the dispersed phase and the melt flow.

Models which are used to simulate the transport of inclusions and/or gas bubbles in liquid melts fall into three categories: (1) quasi single-phase procedure where both liquid melt and inclusions and/or bubbles are handled as one 'mixture' phase [9, 10] (the shortcoming of this approach is that the relative motion between the different phases can only be considered approximately); (2) Eulerian two phase approaches where the dispersed inclusions and/or gas bubbles are considered as a secondary continuous phase for which an additional momentum equation is solved [8, 10-12]; and (3) Eulerian-Lagrangian two-phase models where the melt flow is solved in an Eulerian framework, while the trajectories of the inclusions and/or bubbles are tracked in Lagrangian framework [7, 10, 13-14]. The Euler-Lagrangian method has distinct advantages over the Eulerian-Eulerian method in terms of formulation simplicity, ability to accommodate complicated exchange processes, computer memory requirements, and computational efforts [13]. Therefore, in the present work the Eulerian-Lagrangian method is chosen. The aim of this work is to study the role of coupling and its impact on the occurring melt flow and motion of inclusions and/or bubbles.

2. Model Description

Mass and momentum conservation for an incompressible fluid are given by

$$\nabla \cdot \vec{u} = 0 \tag{1}$$

$$\rho\left[\frac{\partial \vec{u}}{\partial t} + (\vec{u} \cdot \nabla)\vec{u}\right] = -\nabla p + \mu_{eff} \nabla^2 \vec{u} + \vec{F} \tag{2}$$

where $\mu_{eff} = \mu_0 + \mu_t$ is the effective viscosity due to turbulence, for which the standard k-ε model is used. μ_0 is the dynamic viscosity of the melt, ρ is the melt density, $\vec{u}$ is its mean velocity vector, p is the static pressure and $\vec{F}$ is a momentum source term which accounts for the presence of inclusions and/or bubbles as shown in Eq. (9). The turbulent viscosity, μ_t, is defined by

$$\mu_t = \rho C_\mu \frac{k^2}{\varepsilon} \tag{3}$$

with $C_\mu = 0.09$. In the k-ε turbulence model the time-averaged velocity field is solved together with equations for the transport of turbulent kinetic energy, k, and its dissipation, ε,

$$\frac{\partial(\rho k)}{\partial t} + \rho \vec{u} \nabla k = \nabla\left[\left(\mu_0 + \frac{\mu_t}{\sigma_k}\right)\nabla k\right] + G_k - \rho\varepsilon, \tag{4}$$

$$\frac{\partial(\rho\varepsilon)}{\partial t}+\rho\vec{u}\nabla\varepsilon=\nabla\left[\left(\mu_0+\frac{\mu_t}{\sigma_\varepsilon}\right)\nabla\varepsilon\right]+C_{1\varepsilon}\frac{\varepsilon}{k}G_k-C_{2\varepsilon}\rho\frac{\varepsilon^2}{k}\ . \tag{5}$$

In these equations, G_k represents the generation of turbulence kinetic energy due to the mean velocity gradients and $C_{1\varepsilon}$, $C_{2\varepsilon}$, and $C_{3\varepsilon}$ are constants [15]. σ_k and σ_ε are the turbulent Prandtl numbers for k and ε, respectively.

Inclusions and gas bubbles are considered as discrete secondary phases with spherical geometry disperse distributed in the melt. The trajectories of these discrete phases are computed by integrating the following equation of motion in a Lagrangian frame of reference

$$\frac{d\vec{u}_p}{dt}=\frac{18\mu_0}{\rho_p d_p^2}\frac{C_D\,\mathrm{Re}}{24}\left[(\vec{u}+\vec{u}')-\vec{u}_p\right]+\frac{\vec{g}\cdot(\rho_p-\rho)}{\rho_p}\ . \tag{6}$$

Here, $\vec{u}_p$ is the velocity vector, d_p the diameter and ρ_p the density of the considered discrete phase. $\vec{g}$ is the gravity vector and $\vec{u}'$ is the vector of the fluctuating velocity components defined in Eq. 11. The trajectory of an individual discrete object is based on the forces acting as it moves through the flow. The terms on the right-hand side of Eq. 6 represent drag force and buoyancy force. For the drag coefficient, C_D, the following approach is taken [16]

$$C_D=a_1+\frac{a_2}{\mathrm{Re}}+\frac{a_3}{\mathrm{Re}^2}\ . \tag{7}$$

Here, a_1, a_2 and a_3 are constants that apply to smooth spherical inclusions/bubbles over several ranges of Re. The relative Reynolds number, Re, is defined as

$$\mathrm{Re}=\frac{\rho d_p\left|\vec{u}_p-\vec{u}\right|}{\mu_0}\ . \tag{8}$$

The momentum transfer from the discrete phases to the melt is computed by examining their momentum change as

$$\vec{F}=\sum_i^N\frac{18\mu_0 C_D\,\mathrm{Re}}{\rho_p d_p^2 24}(\vec{u}_p-\vec{u})\dot{m}_p\Delta t\ . \tag{9}$$

Here, N is the number of inclusions and/or bubbles in a computational cell and $\dot{m}_p$ is the mass flow rate of inclusions and/or gas bubbles.

The dispersion of the inclusions and/or bubbles due to turbulence in the melt is treated using a stochastic tracking model. This stochastic tracking model includes the impact of instantaneous turbulent velocity fluctuations, $u'(t)$, on the trajectories. The fluctuating velocity components are discrete piecewise constant functions of time. Their random value is kept constant over an interval of time given by the rotation time of an eddy. This rotation time, τ_e, which describes the time a inclusion/bubble spent in the turbulent motion of the considered eddy, is proportional to the discrete phase dispersion rate. Larger values indicate

more turbulent motion in the flow. For the k-ε model the rotation time can be expressed according to [17] as

$$\tau_e \approx 0.3 \cdot k / \varepsilon \ . \tag{10}$$

The values of the fluctuations in 3-dimension u', v' and w' that prevail during the lifetime of the turbulent eddy are sampled by assuming that they obey a Gaussian probability distribution, so that

$$u' = \varsigma \sqrt{\frac{2k}{3}} \qquad v' = \varsigma \sqrt{\frac{2k}{3}} \qquad w' = \varsigma \sqrt{\frac{2k}{3}} \tag{11}$$

where ζ is a normally distributed random number. The discrete phase crossing time is defined as

$$t_{cross} = -\tau \cdot \ln\left[1 - \left(\frac{L_e}{\tau \cdot |u - u_p|}\right)\right] \tag{12}$$

where τ is the discrete phase relaxation time and L_e is the eddy length scale. The inclusion/bubble is assumed to interact with the melt eddy over the smaller of the eddy rotation time and the eddy crossing time. When this time limit is reached, a new value of the instantaneous velocity is obtained by applying a new value of ζ in Eq. (11).

3. Computation Details

The fluid flow and the gas and particle transport are computed in a three-dimensional model domain (Fig. 1) that include a trifurcated submerged entry nozzle (SEN) and a liquid pool of L = 3 m length. The transient simulations describe a steel continuous casting process for thin slabs under the conditions specified in Fig. 1, but without cooling and solidification. Therefore, the viscosity and the density are constant. The material data taken from ref. [5] are consistent with low carbon steel at liquidus. Assuming double-symmetry at the centre planes between the wide and narrow faces of the slab, the computational domain is chosen to be only one quarter of the physical domain. Dispersed particles, i.e. non-metallic inclusions and bubbles, are injected from the top of the SEN, following the flow stream through the nozzle ports into the mould.

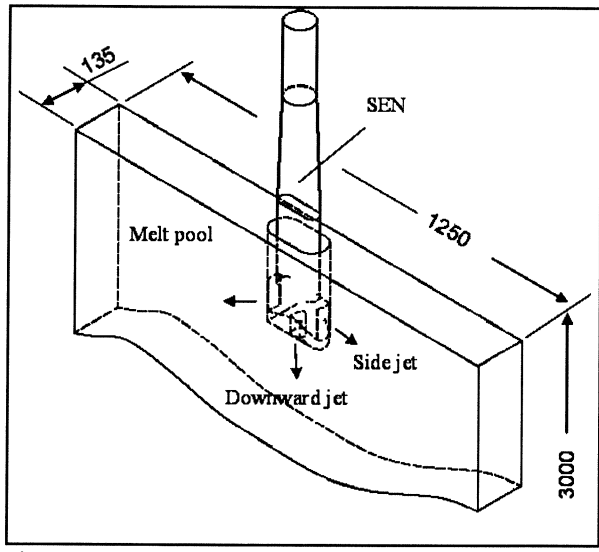

slab width	1250	mm
slab thickness	135	mm
slab length	3000	mm
SEN length	832	mm
SEN submerged depth	160	mm
casting speed	2.5	m/min
steel composition	low carbon steel	
fluid dynamic viscosity	0.00555	kg/(m s)
fluid density	7020	kg/m^3
gravity acceleration	9.81	m/s^2
inclusion density	3700	kg/m^3
inclusion diameter	10;500;1000	µm
inclusion mass flow	9.87E-04	kg/s
gas density	1.6228	kg/m^3
gas bubble diameter	4000	µm
gas volume flow	4	l/min

Fig.1: Considered geometrical and process parameters

Two simulations, one coupled and the other uncoupled are compared in this work. Uncoupled means that the influence of the fluid flow on the movement of inclusions and gas bubbles is considered but not the opposite. On the other hand, a coupled simulation allows the fluid flow to be affected by the presence of the inclusions and/or bubbles. For both simulations the geometry, boundary conditions and material data are the same. The initial conditions were taken from a steady state simulation done before. The computational domain in the liquid pool region has been discretized with a structured mesh and in and around the SEN ports with an unstructured mesh. Non-conforming-mesh interfaces between the structured mesh zone and unstructured mesh zone were defined. The whole grid consists of about 500.000 cells. The time step for the simulation is chosen as small as $\Delta t = 0.3$ ms.

4. Boundary Conditions

Inlet and outlet

The inlet is positioned at the top surface of the $L = 832$ mm long trifurcated SEN. For the melt a constant velocity inlet boundary condition is applied. For the dispersed phases, all the inclusions and bubbles are injected during $t = 100$ ms also at the top surface of the SEN. Three different size classes (10, 500 and 1000 µm) of the non-metallic inclusions and one size of gas bubbles (4000 µm) are introduced. The size and density of the inclusions are chosen to demonstrate typical alumina and alumina clusters in liquid steel. The starting positions are chosen to be uniformly distributed at the inlet surface. Inclusions and bubbles where injected with the same defined inlet melt flow velocity. A constant pressure boundary condition at the bottom of the calculation domain (outlet) is applied. When inclusions or bubbles reach this boundary, they are assumed to leave the domain.

Top surface and walls

The top surface of the liquid melt pool being in contact with the slag is supposed to be flat. Here, a free-slip condition is used. The tapering of the fluid domain is neglected, instead straight moving walls are used with a given constant velocity (casting speed). The boundary

condition between the melt and the SEN wall is also chosen to be no-slip, but the SEN itself is of course considered to be stationary. Particles and gas bubbles are reflecting at moving walls and are modeled as to be caught at the top surface and at SEN walls.

5. Results and Discussions

Overall flow pattern

Fig. 2 shows the stationary velocity field at the central planes of the slab and the nozzle. Here, the impact of inclusions and bubbles on the flow is not considered. The melt flow emerges from the nozzle top (Fig. 2b) and divides through the trifurcated SEN into two side and one center jet. At the nozzle side ports backflow occurs near the upper edges. The main streams of the two side jets bend upwards and build the upper recirculation zone (Fig. 2a). When this flow pattern is strong, inclusions are thought to be carried upwards and to accumulate with the slag. However, if the velocity at the slag surface is too high, the slag itself may be entrapped into the melt and new 'inclusions' occur. Together with the two strong upper vortices, four weak lower vortices occur. They are driven partly by the two side jets, the center jet and the 'moving' walls. The center jet flows directly downwards and is gradually slowed down in the lower part of the melt pool.

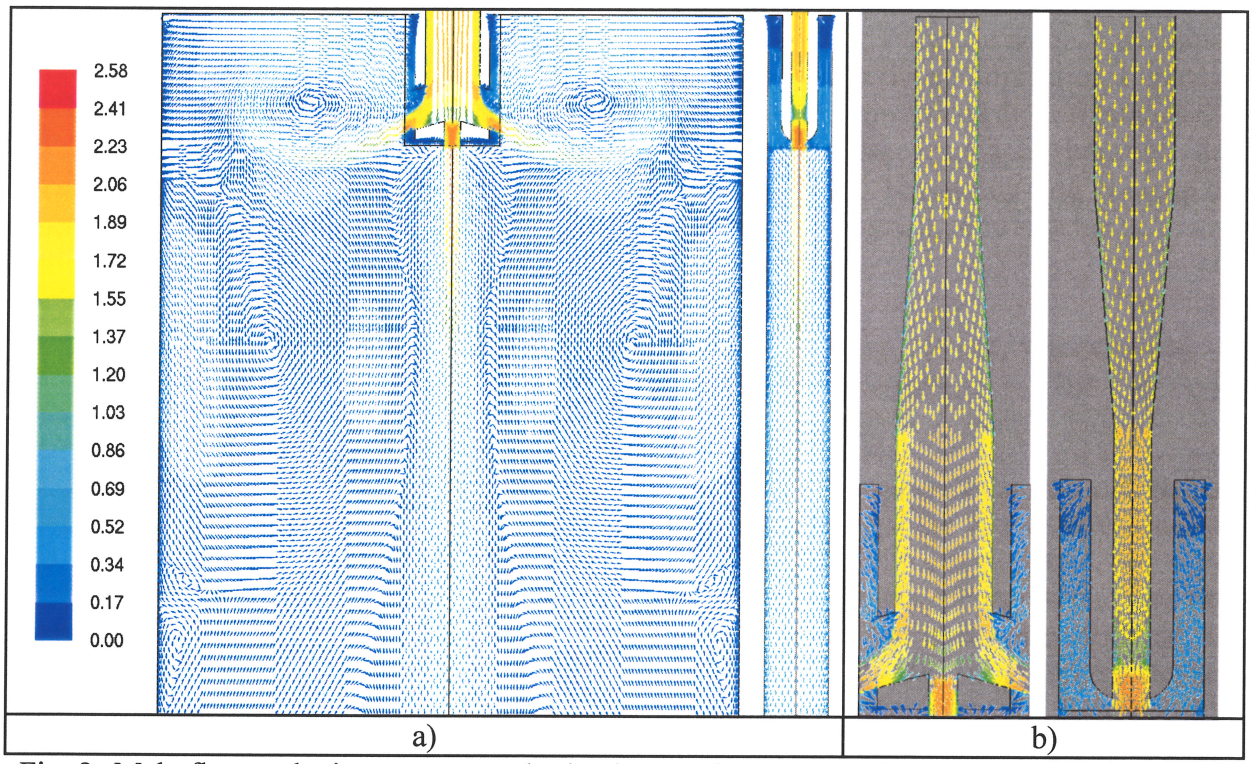

Fig. 2: Melt flow velocity vectors at both planes of symmetry for a) the slab and b) the submerged entry nozzle. The color map shows the magnitude of velocity in m/s.

Motion of non-metallic inclusions and gas bubbles

Fig. 3-5 show the distribution of gas bubbles and inclusions at three different points in time. Bubbles are represented with red dots, inclusions corresponding to their diameters (10,

500, 1000 µm) with green, blue and black dots. From the results it is obvious that the gas bubble and each particle class reveal different flow behaviors. This observation is true for the coupled and the uncoupled simulation. The major difference is found between the motion of the bubbles and the particles. However, also the different size classes of inclusion behave differently. For Example in Fig. 4 the large inclusions reach the top surface first, whereas the smaller ones need much longer time. This is most obvious for the coupled simulation. A special situation is present for some of the medium size inclusions. They have, by accident, been injected near the SEN walls. As the result, they leave the SEN port at a position close to the local backflow (see Fig. 3) and are therefore slow in velocity.

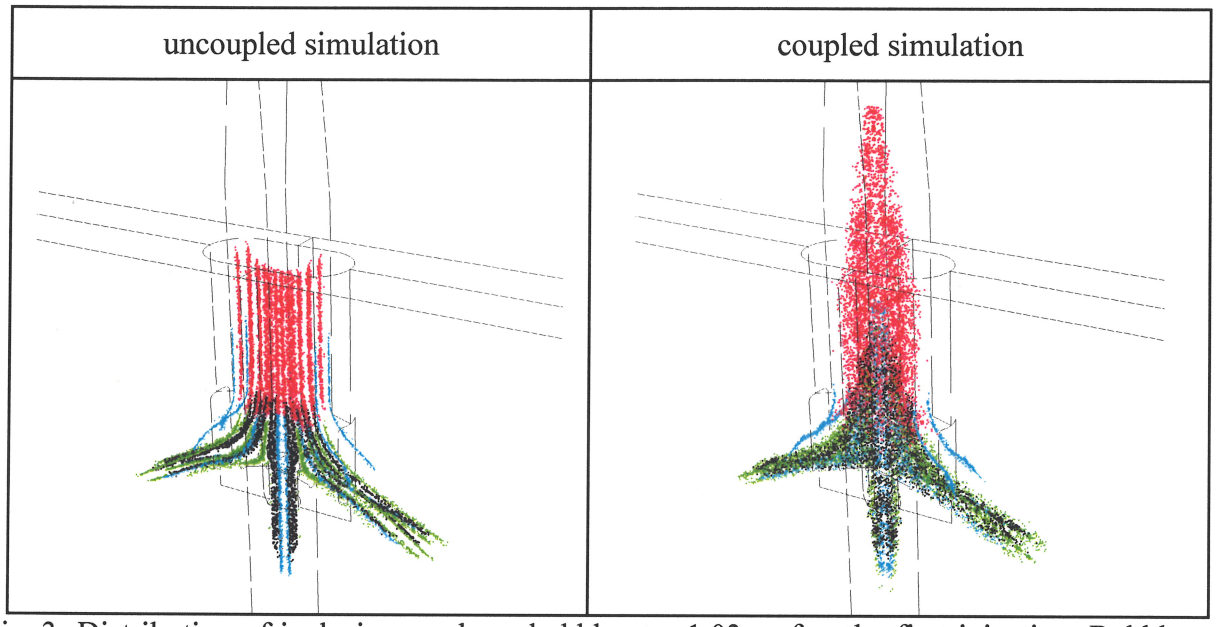

Fig. 3: Distribution of inclusions and gas bubbles t = 1.03 s after the first injection. Bubbles are colored in red, inclusions (10, 500, 1000µm) in green, blue and black.

t = 1.03 s after the injection of gas bubbles and inclusions has been started, the inclusions and bubbles follow the vertical flow stream in the SEN (Fig. 3). Due to the large buoyancy force acting on the bubbles, they are slower compared to the melt flow (and compared to the inclusions). For the coupled simulation, these slower bubble velocities lead to a deceleration of the melt flow, whereas the melt flow is unchanged for the uncoupled case. The resulting difference in the velocity profile across the nozzle at certain heights in the symmetry plane is shown in Fig 6. The rise of the bubble relative to the melt flow and the resulting deceleration of the melt for the coupled case are more pronounced in the center part of the SEN. Thus, 'w'-shape velocity profiles form. Due to these 'w'-shaped velocity profiles, the inclusions and bubbles are more dispersed compared to the more or less flat velocity profile for the uncoupled case.

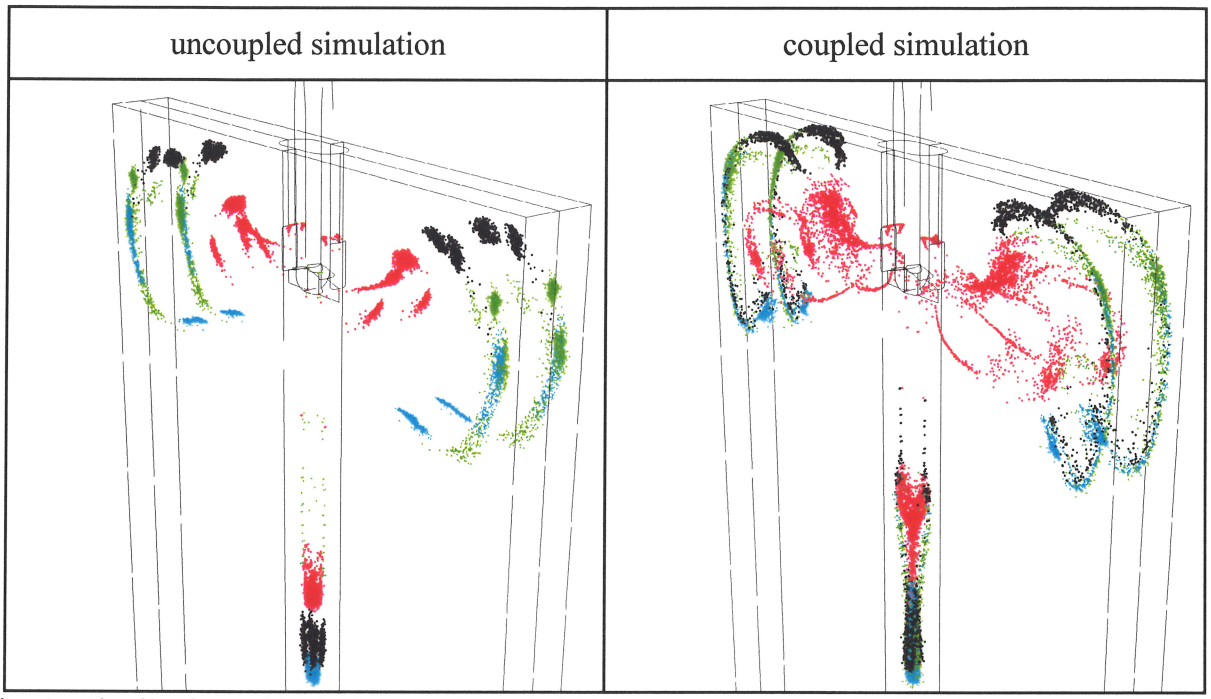

Fig. 4: Distribution of inclusions and gas bubbles t = 1.78 s after the first injection. Bubbles are colored in red, inclusions (10, 500, 1000µm) in green, blue and black.

Fig. 4 shows the difference after t = 1.78 s when inclusions and bubbles are out of the SEN. The inclusions following the side jets bend upwards similar as the melt flow does. It turns out that with the consideration of bidirectional momentum exchange (coupled) the inclusions and bubbles can rise more easily upwards and thus reach the top surface earlier. The reason for that is that buoyancy forces acting on bubbles and inclusions accelerate the upwards melt flow near the narrow mold faces. However, for the coupled case only a part of the bubbles move towards these faces. The main part is directly moving upwards, namely right through the rotation axis of the upper eddies where no downward motion hinders the rise of the bubble. For the uncoupled case all bubbles rises close to the SEN in countercurrent with the downwards motion of the upper eddies.

Inclusions and bubbles that follow the middle jet are brought very quickly downwards, especially in the first two seconds. Due to the 'size dependent' drag force, bubbles and inclusions are fanned out according to their size. However, for the uncoupled situation there exists a point in time, where the drag force on the bubbles/inclusions is balanced with the buoyancy force. From then on the bubbles/inclusions are captured where they are without a change to ever move from their positions. Such a situation is shown in Fig. 5. For the coupled case, the bubbles/inclusions traveling with the middle jet slow down their downwards motion and then rise upwards mainly at the outer boundary of the jet. This upwards motion of the bubbles/inclusions slows down the velocity of the jet at its periphery. In consequence, due to mass conservation the cone of the jet is slightly accelerated. The described phenomena demonstrate that the results of the uncoupled and the coupled simulation are quite different, especially if details are important.

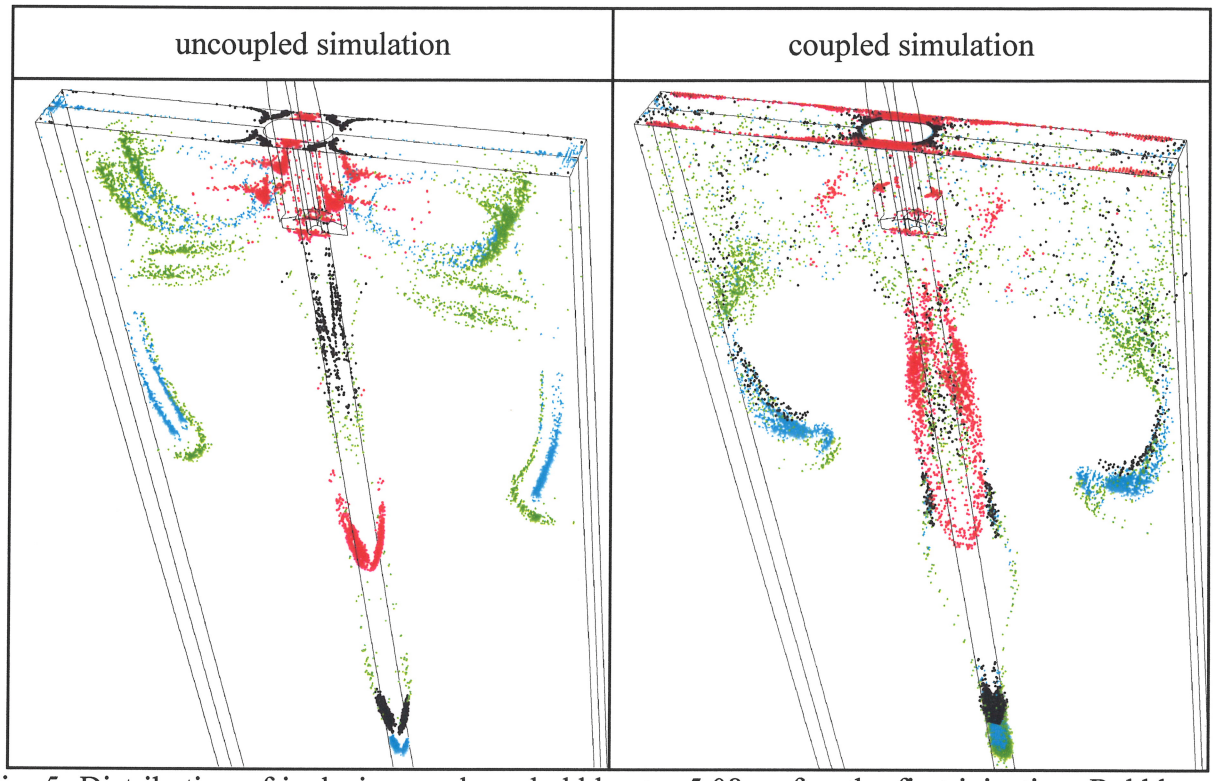

Fig. 5: Distribution of inclusions and gas bubbles t = 5.08 s after the first injection. Bubbles are colored in red, inclusions (10, 500, 1000μm) in green, blue and black.

Another difference is obvious, by looking on the overall distribution of bubbles/inclusions (Fig. 5). t = 5.08 s after the injection of bubbles and inclusions has been started they are much more dispersed in the upper circulation zone and at the top surface for the coupled simulation compared with the uncoupled.

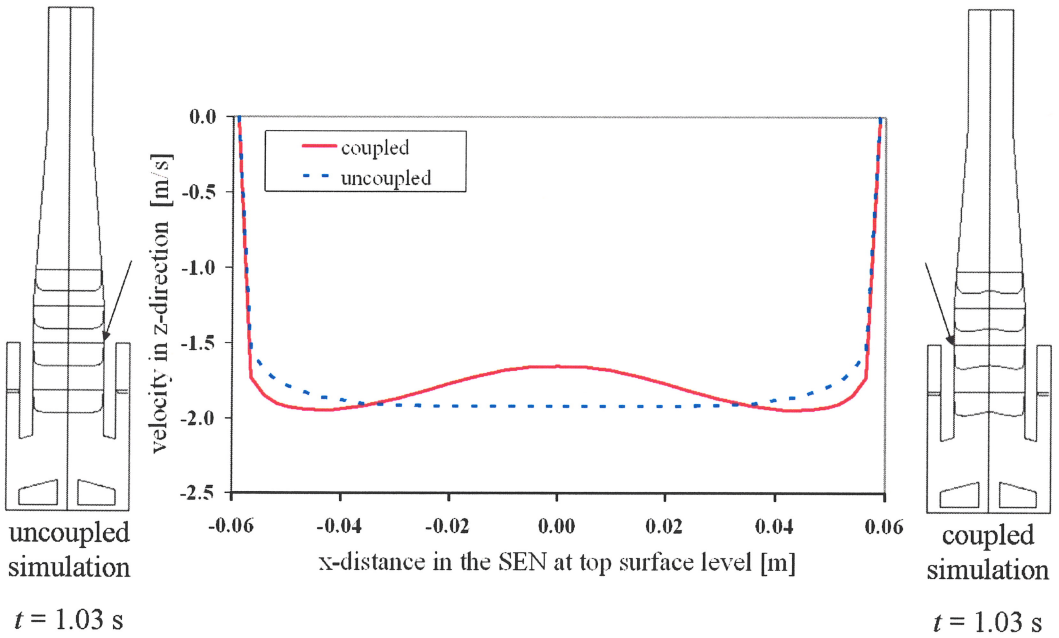

Fig. 6: Comparison of the velocity profiles at certain heights within the SEN, t = 1.03 s after the start of particles/bubbles injection.

6. Conclusions

Simulations with an Eulerian-Lagrangian model for the transport of the non-metallic inclusions and gas bubbles in the SEN and the melt pool of a steel continuous caster has been performed. The comparison of a simulation which takes into account the impact of the melt flow on the motion of inclusions/bubbles with a second simulation which accounts in addition for the back influence indicate that coupling is essential for a proper prediction of inclusion/bubble trajectories. This is especially true when large gas bubbles are present. This conclusion is based on the following findings:

1. The coupled simulation shows that during gas injection the downward melt velocity in the center of the SEN is slower compared to the uncoupled.
2. The uneven velocity profile in the nozzle causes a wider spreading of inclusions and bubbles within the SEN and also in the mold region.
3. Inclusions and gas bubbles are more dispersed in the melt pool and at the top surface using bidirectional coupling.
4. The melt flow is significantly affected by the strong buoyancy force acting on large gas bubbles.

Acknowledgements

This work is financially supported by Austrian Christian-Doppler (CD) Research Society, VOEST-Alpine Industrieanlagenbau GmbH&Co and RHI Refractories, in the frame of CD-Laboratory – *Multiphase Simulation of Metallurgical Processes* for which the authors kindly acknowledge. The authors are also grateful to Dr. Braun and Dr. Pelzer with FLUENT Deutschland GmbH, Darmstadt, Germany, for their excellent technical assistance.

References

[1] B. G. Thomas, Continuous Casting, in: K. O. Yu (Eds.), Modeling for Casting and Solidification Processing, Marcel Dekker Inc., New York, 2002, pp. 499-539.

[2] L. Zhang and B. G. Thomas, Iron Steel Inst. Jpn. Int. 43 (2003) 271-291.

[3] A. Ramos-Banderas, R. Sanchez-Perez, R.D. Morales, J. Palafox-Ramos, L. Demedices-Garcia and M. Diaz-Cruz, Metall. Mat. Trans. 35B (2004) 449-460.

[4] Q. Yuan, S. Sivaramakrishnan, S.P. Vanka and B.G. Thomas, Metall. Mat. Trans. 35B (2004) 967-982.

[5] Q. Yuan, B. Zhao, S. P. Vanka and B. G. Thomas, Steel Res. Int. 76 (2005) 33-43.

[6] Q. Yuan, B.G. Thomas and S.P. Vanka, Metall. Mat. Trans. 35B (2004) 685-702.

[7] Q. Yuan, B.G. Thomas and S.P. Vanka, Metall. Mat. Trans. 35B (2004) 703-714.

[8] M. Javurek, P. Gittler, R. Roessler, B. Kaufmann, H. Presslinger, Steel Res. Int. 76 (2005) 64-70.

[9] B. G. Thomas, X. Huang and R.C. Sussman, Metall. Mat. Trans. 25B (1994) 527-312.

[10] D. Mazumdar and R. I. L. Guthrie, Metall. Mat. Trans. 25B (1994) 308-312.

[11] A. Mukhopadhyay, E. W. Grald, K. Dhanasekharan, S. Sarkar and J. Sanyal, Steel Res. Int. 76 (2005) 22-32.

[12] M.P. Schwarz, Appl. Math. Modelling 20 (1996) 41-51.

[13] S.T. Johansen and F. Boysan, Metall. Trans. 19B (1988) 755-764.

[14] A. Alexiadis, P. Gardin and J. F. Domgin, Metall. Mat. Trans. 35B (2004) 949-956.

[15] B. E. Launder and D. B. Spalding. Lectures in Mathematical Models of Turbulence. Academic Press, London, England, 1972.

[16] S. A. Morsi and A. J. Alexander, J. Fluid Mech. 55(2) (1972) 193-208.

[17] B. J. Daly and F. H. Harlow. Phys. Fluids 13 (1970) 2634-2649.